Applied Surface Science 709 (2025) 163734

Contents lists available at ScienceDirect

Applied Surface Science

journal homepage: www.elsevier.com/locate/apsusc

Full Length Article

Ion-beam channeling in a single-surface modified Si membrane

Dustin Andersen [a,*], Radek Holeňák [b], Saba Tabean [a], Eleni Ntemou [b], Tom Wirtz [a], Gerhard Hobler [c], Daniel Primetzhofer [b], Santhana Eswara [a,*]

[a] Advanced Instrumentation for Nano-Analytics (AINA), Luxembourg Institute of Science and Technology, 41 rue du Brill, L-4422 Belvaux, Luxembourg
[b] Department of Physics and Astronomy, Uppsala University, Box 516, S-751 20 Uppsala, Sweden
[c] Institute of Solid-State Electronics, TU Wien, 1040 Vienna, Austria

ARTICLE INFO

Keywords:
Silicon
Ion implantation
Amorphized surface
Ion-beam analysis
Ion channeling
ToF-MEIS

ABSTRACT

The scattering and energy distributions of ions ($^{22}Ne^{+}$ and $^{4}He^{+}$) transmitted through a Ga implanted single-crystal Si (0 0 1) membrane are studied both experimentally and with a Monte-Carlo binary collision approximation code (IMSIL). The membrane is studied in both a [0 0 1] orientation to the ion beam as well as an inverted orientation. Both the scattering and energy distributions of the transmitted particles reveal a strong dependence on the membrane orientation due to the amorphization of the Si surface. When ions well-aligned to the [0 0 1] axis first encounter the crystalline layer, they primarily travel along the axial channel before being randomly scattered by the amorphous surface layer, yielding a random scattering distribution. Alternatively, when the trajectories are initially randomized by the amorphous surface, a large fraction of the ions are directed to higher energy-loss pathways upon entering the crystal, such as planar channels and random trajectories. The resulting scattering distribution reveals the crystalline features of the sample (e.g., star pattern) but with a larger energy spread and a higher average energy loss than the former case. This work aims to extend transmitted ion beam imaging and ion energy-loss analysis in the keV range to complex heterostructures with both crystalline and amorphous regions.

1. Introduction

As ions travel through a material, they transfer some of their energy to the atomic nuclei and electrons of the material, and the rate at which the material absorbs the particle's energy is called the stopping power [1]. In the case of nuclear interactions (which typically dominate at lower energies [2]), energy is transferred between the projectile ion and the target nuclei in the form of elastic scattering events, which can lead to permanent displacement of the lattice atoms, collision cascades, sputtering, and eventually, amorphization for crystalline samples [3]. The projectile can also inelastically transfer energy to the electrons of the material, and the electronic stopping power is strongly dependent on the ion velocity [4]. In particular, charge-exchange with the incident ion, promotion of electrons to higher states (e.g. valence to conduction band), induced plasmon resonances [5], and generation of secondary electrons, can all play a role in slowing the incident particle. However, the mathematical separation of the nuclear and electronic stopping powers relies on projectile-target interaction potentials derived from the instantaneous electronic ground state (e.g., the adiabatic approximation) [6], which is typically only valid for particle velocities well above the Bohr velocity (i.e. well above the electron orbital velocities).

In amorphous samples, and for random trajectories within crystalline samples, incident ions interact with the sample atoms at random intervals and impact parameters. However, if an incident ion beam is well aligned to the symmetries of a crystal lattice (up to a critical acceptance angle [7–9]), then the ions can be steered into channels, where potential wells created by the periodic structure of the crystal can gently steer particles back to the center of a channel if they have a sufficiently low transverse velocity, leading to reduced nuclear stopping power [7,10]. The highest symmetry directions within a crystal are the zone axes, where many low-order (e.g. {1 0 0}, {1 1 0}, etc.) atomic planes intersect, though ions can channel along a large number of even higher-order axes and planes [11]. Due to the significantly reduced nuclear stopping in the channeling condition, electronic stopping becomes of much higher importance. The ions traveling in these channels take on an oscillatory motion as they are repeatedly steered back to the center of the channel by the repulsive forces at the sides of the channels, and due to the

* Corresponding authors.
E-mail address: dustin.andersen@list.lu (D. Andersen).

https://doi.org/10.1016/j.apsusc.2025.163734
Received 29 January 2025; Received in revised form 20 May 2025; Accepted 3 June 2025
Available online 4 June 2025

relationship of these repulsive forces with the impact parameter, a variety of initial impact parameters lead to similar trajectories. These converging trajectories result in peaks in the particle flux within the crystal, and for very thin crystals result in characteristic rainbow channeling patterns [12,13]. In the presence of defects (i.e. vacancies, interstitials, dislocations, stacking faults, and volume defects) [14] or due to thermal vibrations of the crystal lattice [15], even well channeled ions may eventually be dechanneled.

Closely related to channeling is blocking. When a particle scatters from a lattice site into a crystallographic direction (i.e., axial or planar), then its trajectory is necessarily aligned with other lattice sites, preventing the particle from continuing in that direction. This condition leads to a reduction of, e.g., backscattering intensity along crystallographic directions [16]. However, defects in the crystal lattice (e.g. interstitial atoms) can potentially scatter ions into channeling conditions [17].

Finally, the surface quality of a crystal can influence the ion trajectory as it enters the crystal, potentially leading to significant scattering of the beam before channeling can occur [18]. Indeed, screening oxides have been used in the semiconductor industry in ion implantation to avoid channeling and achieve a shallower implantation profile by randomizing the direction of the ions as they enter the crystal [19]. However, for certain orientations of the incident beam (i.e. off-axis), this screening layer can actually increase the implantation depth as the random surface scattering redirects the incident ions into channels [20,21]. Holeňák et al. recently showed that the earlier redirection of ions into channeling conditions by an amorphous layer – for simulations of transmitted ions with an off-axis beam alignment – leads to reduced ion energy loss [22].

This work compares experimental and simulation results for ion channeling in a thin membrane sample with a heavily amorphized surface for incident ion velocities just below the Bohr velocity ($v_0 = 2.19 \times 10^6$ m/s). We explore the influence of inverting the sample to place the amorphous layer at the top of the membrane versus the bottom of the membrane, highlighting the impact of limiting the region of ion-induced beam damage to just the surface layer of the crystal (see Mikšová et al. [23] for an example of He^+ ion channeling in a thin Si (1 0 0) sample with ion-beam induced damage across the entire layer thickness). Furthermore, we explore the evolution of the scattering and energy distribution as a function of depth in the sample via simulation to better understand the influence of the position of the amorphous layer. This work aims to extend transmitted ion beam imaging and ion energy-loss analysis in the keV range to complex heterostructures with both crystalline and amorphous regions (e.g. semiconductor devices, thin film coatings, and geological specimens). At these lower energies, ion-beam probe sizes down to 0.5 nm can be formed (e.g. the helium ion microscope – HIM [24]), thus allowing for nanometer scale transmitted ion-beam analyses of samples (see [25] for an example of scanning transmission ion microscopy on HIM).

2. Methods

2.1. Experimental samples

The samples used for this work were 200 nm thick single-crystal Si membranes with a tensile strain to ensure that the membrane remained extremely flat for the channeling experiments. Membranes with similar specifications were purchased from another vendor and also used as a reference for the pristine crystal. The channeling results from the pristine membranes are shown in Fig. A1 of Appendix A. The samples came in the form of square chips (5 × 5 × 0.2 mm Si support frame) with the surface of the membrane being parallel to the (0 0 1) plane and the edges of the chip being parallel to the {1 1 0} family of planes (see the reference axes in Fig. 1). The membrane windows were 1 × 1 mm.

The top side of the membranes was implanted with $^{69}Ga^+$ ions using a 30 keV ^{69}Ga liquid metal ion source (LMIS) on a Thermo Fisher Scientific SCIOS dual-beam FIB-SEM, to achieve a dose of 1×10^{16} at·cm^{-2}. At 30 keV, Ga has a projected range of about 28 nm in Si (according to simulations performed with TRIM) [26]. From the ion depth profile as obtained by TRIM, it was calculated that the Ga reached a peak concentration of approximately 8 % at the projected range for the implanted dose. This high Ga dose created an amorphous surface layer on one side of the sample, while leaving most of the volume of the sample undamaged [27]. It is expected that there will also be a several nanometer thick interfacial transition between the amorphized surface and the crystalline region [28]. From the TRIM calculations, the number of target displacements can be calculated as a function of depth, which for an amorphization threshold of 1.3×10^{16} displacements·cm^{-3} [29] (0.26 displacements per atom) gives an amorphous layer thickness of 48 nm. Furthermore, the high implantation dose is also expected to sputter away some of the surface layer. Based on a sputter yield of 2.28 for 30 keV Ga into Si, 4.5 nm (or just over 2 %) of the membrane thickness would be removed.

After implantation, the sample was annealed under high-vacuum in a rapid thermal processing system at 700 °C for 1 min with a 30-minute linear ramp-up and ramp-down to avoid thermal shock. The original purpose of the anneal was to restore crystallinity to the damaged area of the membrane while retaining the implanted Ga [30]. However, Rutherford backscattering spectrometry (RBS) measurements after the experiments shown in this paper indicated that there was very little Ga remaining within the sample (similar loss of Ga implanted in Si during annealing has been reported in literature [31]). The RBS measurements also revealed some small amount of Pt at the sample surface, likely coming from organometallic precursor contamination within the

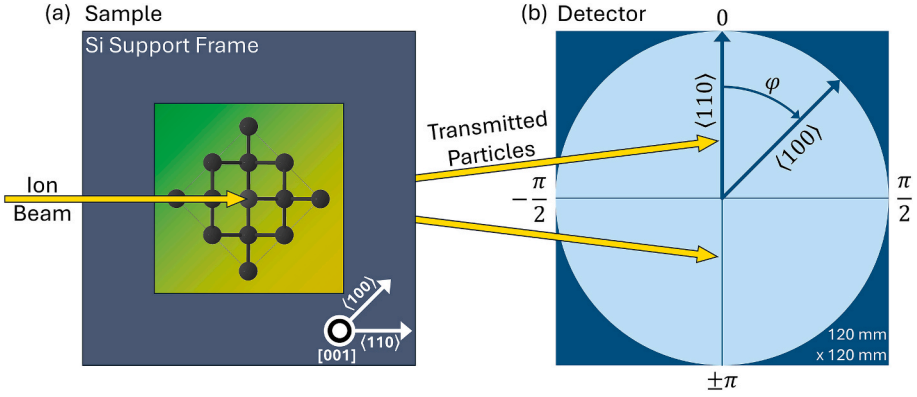

Fig. 1. Schematic of the experimental setup within the ToF-MEIS showing (a) the sample with an inlay of the Si(100) crystal lattice as seen from the perspective of the beam, and (b) the detector. The angles shown on the detector are used as a reference for the plotting and the Miller indices correspond to the direction in the crystal projected onto the detector.

implantation chamber, as is common on dual-beam FIB-SEMs equipped for nanofabrication. In summary, the amorphous layer is estimated to have a thickness as high as 25 % of the layer but is likely much thinner due to both the sputtering of the top surface and the post-implantation anneal.

2.2. Experimental setup

The samples were measured using the Time-of-Flight Medium Energy Ion Scattering spectrometry (ToF-MEIS) facility at Uppsala University. This system is based on a Danfysik ion implanter model 1090, capable of creating beams of nearly any element with accelerating voltages up to 350 kV. For our work, we used beams of both $^{4}He^{+}$ and $^{22}Ne^{+}$ at 50 keV and 280 keV, respectively. While ^{22}Ne is 5.5 times more massive than ^{4}He, the chosen accelerating voltages give approximately the same ion velocity of $\sim 1.6 \times 10^{6}$ m s^{-1}, which is slightly below the Bohr velocity ($v_0 = 2.19 \times 10^{6}$ m/s). The beamline additionally has a synchronized chopper-pulser configuration capable of creating beam pulses down to 1 ns. Before reaching the sample, the beam can be focused (to a spot size of <1 mm at the sample plane with a beam divergence better than 0.056° [32]) and is deflected a few degrees to remove any neutrals. Inside the main chamber, the system has a 120 mm diameter microchannel plate with delay-line detector (MCP-DLD) from Roentdek with a temporal resolution of <250 ps, which can be moved around the sample at a fixed distance of 290 mm from the center of the chamber to allow for both forward and backscattering measurements. The time delay between pulsing and detection is measured with a time-to-digital converter (TDC) with a temporal resolution of <100 ps. A detailed discussion of the physical layout and electronic systems of the ToF-MEIS system can be found in Linnarsson et al. [33], as well as its updated capabilities in Sortica et al. [34] and Ntemou et al. [35].

Within this work, the MCP-DLD detector was exclusively placed directly behind the sample in the transmission mode to collect the transmitted ions/neutrals using a methodology developed by Lohmann et al. [36], with the beam aligned along the [0 0 1] direction of the Si crystal. The pulsing and chopping configuration of the ToF-MEIS system was used to achieve a pulse width of approximately 1 ns, which was measured from the direct beam and verified throughout the experiments by measuring the width of the photon peak. Photons generated by beam interactions with the sample arrive at the detector after ~1 ns (much faster than the ions) and can be used as a reference point in the data to determine the precise time-of-flight [37]. It should be noted that in the images produced by the DLD there are several lines that appear as an artifact of the data processing that are not part of the data (see Fig. A2 in Appendix A).

Over the course of the experimental measurements, the sample was exposed to approximately 10^{9} at·cm^{-2} of He^{+} ions and an equivalent dose of Ne^{+} ions. These values are well below the expected threshold for significant damage to the sample for either He^{+} or Ne^{+} ions in these energy ranges, and so it is not expected that the ion induced damage from the measurement beams has influenced the experimental results.

2.3. Simulation

The IMplant and Sputter sImuLator (IMSIL) code [38] used in this work is a Monte Carlo binary collision approximation (BCA) code developed and maintained by Gerhard Hobler at TU Wien. This code is capable of simulating ion scattering in targets with up to one crystalline region and an arbitrary number of amorphous regions. Full details of the code can be found in the IMSIL manual (available online at [39]). The virtual sample used for this work consists of two layers: a diamond-cubic Si crystalline layer (designated 'C') of 175 nm thickness with the (0 0 1) plane normal to the incident direction of the beam and a 25 nm thick amorphous Si layer (designated 'A'). The virtual sample was oriented in both C-to-A (or CA) as well as A-to-C (or AC) configuration with respect to the incident beam. An additional virtual sample consisting of only a 200 nm thick crystalline silicon layer was also simulated under the same conditions for reference.

The incident beam conditions were the same as the nominal ones of the experiments (i.e., 50 keV $^{4}He^{+}$ and 280 keV $^{22}Ne^{+}$). With a starting beam divergence of 0°, 10^{5} ions were simulated per sample, with the ions hitting the sample within the size of a crystal unit cell and being tracked until the point where they left the sample, or their energy fell below 10 eV. In the crystalline layer, collision partners were selected from the target atoms, assuming Gaussian displacements from the lattice sites according to the Debye model with a Debye temperature of 490 K [38]. In the amorphous layer, the free flight paths were chosen according to an exponential distribution with a mean value guaranteeing that no collisions with scattering angles larger than 0.01° were missed [40]. For the treatment of the scattering events, the ZBL interatomic potential [41] was used, and for electronic stopping a mixed local/nonlocal model as described in Ref. [42] was used. Electronic energy-loss straggling was neglected. Full trajectories (i.e., one datapoint for each scattering event of each ion) including direction cosines and energies as well as histograms describing the ions as they exit the virtual sample were recorded as the output of the simulation.

2.4. Data treatment

The ToF data from the experiments at the ToF-MEIS system at Uppsala were pre-processed to remove extraneous events (see Appendix B for details), and then shifted by an offset C_{ToF}, which was chosen as the center of the photon peak (this offset represents the time between the electronic pulse signal and the arrival of the ions at the sample). Data points with a negative ToF relative to C_{ToF} were dropped from the dataset. The time-of-flight data was then converted to particle energy according to Eq. (1).

$$E = \frac{1}{2} m \left(\frac{d}{t_{ToF}} \right)^{2} \tag{1}$$

Where d is the distance from the sample to the detector, m is the mass of the particle, and t_{ToF} is the particle flight time. The additional flight time due to the scattering angle was not accounted for, however, this only results in a maximum of 2 % error in ToF at the edge of the detector (i.e., at the maximum scattering angle). The converted data was collected into normalized energy histograms, where the weight of each count was set to according to a power-law relation (seen in Eq. (2) below) to account for histogram bins at higher energies corresponding to smaller time windows (e.g. for 290 mm flight distance and ^{22}Ne, $\Delta E = 1000$ eV is equivalent to $\Delta t = 53$ ns at 10 keV, but only $\Delta t = 1.56$ ns at 100 keV).

$$w_{count} = \left(\frac{E}{E_0} \right)^{1.5} \tag{2}$$

Where E is the energy of the count and E_0 is the beam energy. Finally, the data was placed into evenly spaced energy slices (10 keV slices for Ne; 0.75 keV & 1 keV slices for He) and binned according to its XY coordinates (128 × 128 pixels) to create a series of energy-dispersive scattering images. The methodology of energy slicing used in this work builds upon the methodology developed by Holeňák et al. [43].

For the simulation data, the position and trajectory output of IMSIL at the exit surface of the sample was used to determine the ultimate position of the particles on the detector plane according to Eq. (3) below, and any data points outside of a 60 mm radius were discarded, as they would be outside of the detector area in the experiments.

$$x_{DLD} = x_{sample} + u_x \frac{d}{u_z}$$

$$y_{DLD} = y_{sample} + u_y \frac{d}{u_z} \tag{3}$$

Where x_{DLD} is the x position on the MCP-DLD detector, x_{sample} is the x position on the sample as the ion leaves the target, u_x is the x direction cosine, u_z is the z direction cosine, and d is the distance from the sample to the detector (290 mm for the experimental setup). After this initial step, the data was treated identically to the experimental data. It should be noted that within our simulations, the lateral distances traveled by the particles within the sample were negligible compared to the detector distances, and thus the primary contribution to the detector impact position comes from the direction cosines.

Finally, for the full-trajectory simulations, the instantaneous trajectory of each particle was determined at 1 nm intervals along the depth of the virtual sample. This dataset was collected into two representations. The first is simply a depth series of particle positions, detector scattering images, and energy distributions, which are shown as videos in Appendix C (NOTE: see online version of the manuscript for videos). For the detector images, the instantaneous trajectory at each depth was transformed according to the same calculations as the "exit-plane only" simulation results (i.e., Eq. (3)), as if the particles had exited a sample whose thickness was that depth. The second representation is a set of graphs with depth as the x-axis, and particle position, an angular spectrogram, detector-plane scattering deviation, and average particle energy as the y-axes (Fig. 6).

Here the detector-plane scattering deviation is defined as the standard deviation of the radial impact position of the particles on the virtual detector. While the angular distribution of the particles could be directly accessed from the simulations, the scattering deviation acts as a proxy that is in units directly comparable to the experimental results. It should be noted that the highest scattering angles are excluded, as they fall outside of the detector area. The angular spectrograms were created by converting the crystal trajectories to polar coordinates, and then binning by angle (3° bin size) for each depth. The crystallographic direction is used to clarify how the angle corresponds to the crystal lattice.

3. Results and discussion

3.1. Experimental and simulation (exit-plane only) results

The results shown in this section are only from the experiments and simulations performed with the $^{22}Ne^{+}$ ion beam, but similar results were found with the $^{4}He^{+}$ ion beam (see Fig. S1-4 in the *Supplementary Material* – Appendix D). Note that for ease of viewing, the color scale is normalized to each subfigure.

Fig. 2 shows the experimental results for the AC configuration of the sample (i.e., with the amorphized side facing the incident beam) for the 280 keV $^{22}Ne^{+}$ ion beam. The pattern seen in Fig. 2a(i) is from stray particles (e.g., scattered off an aperture edge) passing around the sample holder. The majority of the ions which have passed through the sample have lost at least ~ 40 keV. The highest energy transmitted particles (see Fig. 2a(ii)) are concentrated near the center of the transmission pattern and correspond to the ions which have primarily channeled along the [001] zone axis. The star-like pattern corresponds to particles channeled along the {220} family of planes ({220} is the first subset of {110} in the diamond cubic structure of Si that is not subdivided by another plane of atoms). By Fig. 2a(v), the secondary set of arms for the star pattern emerge, corresponding to particles channeled along the {400} family of planes (similarly, {400} is the first subset of {100}). Finally, the ions which have lost the most energy are those from random trajectories. A subset of these trajectories are blocked by the crystal lattice, which can be seen in Fig. 2a(vii), where the {220} blocking pattern appears, followed by the {400} blocking pattern emerging in Fig. 2a(viii).

The energy spectrum (Fig. 2b) shows a somewhat flat plateau, indicating a multimodal distribution, with a weighting towards lower energies (i.e. higher energy loss trajectories). While the amorphous surface layer initially scatters the particles into random directions, some ions are directed into the channels. These various trajectories are each associated with their own energy-loss distribution, which in order of increasing energy-loss are: [001] axial channel, {220} planar channels,

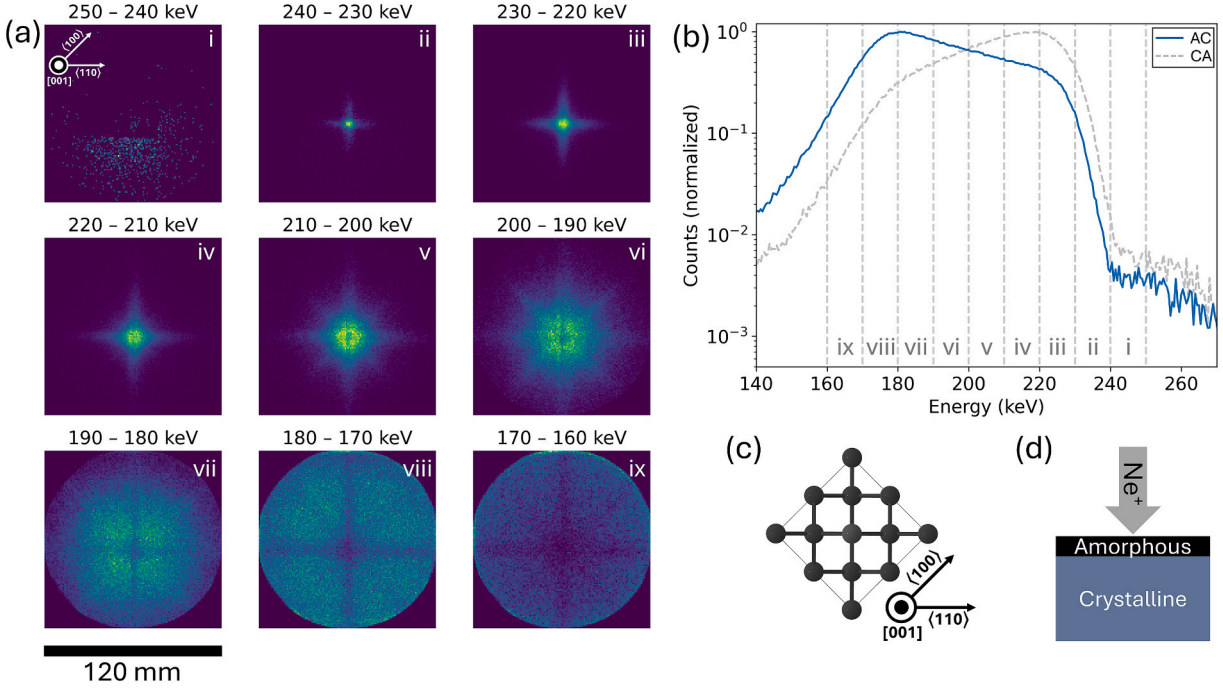

Fig. 2. Experimental results for the AC configuration with 280 keV $^{22}Ne^{+}$ beam. (a) Each sub-figure represents a 10 keV bin from (b) the energy spectrum (500 eV binning); dashed grey line in (b) is CA configuration shown here for comparison. Some of the counts in (i) are from stray particles which passed around the sample. A clear transition from channeling to blocking can be observed between (vi) and (vii). NOTE: the color scale is unique to each subfigure. (c) Shows the crystal structure of the Si sample as seen from the perspective of the beam. (d) Shows the orientation of the sample in cross-section relative to the beam.

{4 0 0} planar channels, and random scattering. However, it is clear from the corresponding images for each energy bin that there is significant overlap in the energy-loss from each type of trajectory.

Fig. 3 shows the IMSIL results for the same AC configuration of the sample. A very similar set of patterns emerges, though the simulated pattern shows several details (e.g. distinct ring pattern and bifurcation of the arms of the star) which are not present in the experimental pattern. We believe these features are due to the oscillations of the ions within the channel, where trajectories closer to the edges of the channel (and thus corresponding to a higher angle) experience greater energy loss. The missing pattern features can be partially explained by a relatively low sample quality in the experiment, as these ring patterns have been seen clearly in previous work on Si thin membranes at the Uppsala ToF-MEIS system [43]. The pristine samples used in this experiment show a channeled spot with a full-width half-maximum (FWHM) value of over 10 mm and the pristine sample from another vendor shows a spot with a FWHM of 5 mm, while the virtual sample shows a spot with a FWHM of only 1.5 mm (see Fig. A1 in Appendix A). Furthermore, the limitations of the physical beam (~1 mm diameter and <0.056° divergence) will also impact the detector pattern quality compared to the simulated beam (5.43 Å square and 0° divergence).

Overall, the energy spectra in Fig. 2b and Fig. 3b are quite similar, with the transmitted particle energies forming a plateau-like distribution, and a similar peak width between the experimental and simulation results. However, in the experiment, the trajectories appear to be weighted more towards the higher energy-loss trajectories than in the simulation, where the plateau is quite flat (except the bump around 190 keV, which corresponds to random trajectories). This energy distribution also consistent with the perfect crystallinity of the virtual sample compared to the lower-quality real sample.

Fig. 4 shows the experimental results for the CA configuration of the sample (i.e., with the crystalline side facing the incident beam) for the 280 keV $^{22}Ne^{+}$ ion beam. Again, the majority of the ions which have passed through the sample have lost at least ~40 keV. None of the patterns show crystalline features. Since the crystal is encountered first, it is likely that the scattering distribution resembled Fig. A1a before reaching the amorphous layer, where the average angle of the scattering distribution greatly increased. Thus, it appears that the ions primarily traveled along the [0 0 1] axial channel of the Si lattice and were then randomly scattered by the amorphous layer on the exit surface. In the CA configuration, the energy spectrum (Fig. 4b) is weighted towards higher energies, but still shows a plateau-like distribution. While the detector scattering pattern appears more random for the CA configuration, the overall spread of the energy distribution is slightly lower than that of the AC configuration. This apparent discrepancy in scattering pattern and energy distribution comes from the trajectories the ions follow for the majority of the sample thickness, which is discussed in Section 3.2 below.

Fig. 5 shows the IMSIL results for the CA configuration of the sample. The scattering patterns in Fig. 5a are qualitatively similar to the experimental results shown in Fig. 4a. However, the simulated ions have lost significantly less energy on average (Fig. 5b) than in the experimental results (Fig. 4b). The crystal quality could be a significant factor in why the experimental energy spectrum has a more plateau-like distribution compared to the simulation, as it can be noted that the pristine sample already shows some features of the star pattern (Fig. A1a), and thus some ions are already traveling along planar channels.

3.2. Full trajectory simulation results

The full trajectory IMSIL simulation results are shown in full as a depth series of particle positions, detector scattering images, and energy distributions in Appendix C and are summarized in Fig. 6. Fig. 6a,b show 2D histograms of the full trajectories of the ions through the sample as viewed from the [1 1 0] direction for both (a) the AC configuration and (b) the CA configuration. The stripes which can be seen across the depth of the histograms correspond to channeled ions. The stripes near the center of the width correspond to ions traveling in [0 0 1] axial channels (with superimposed {2 2 0} planar channeling). For the AC configuration, the ions are initially scattered randomly by the amorphous surface layer, but many are redirected into channels upon entering the crystal. For the CA configuration, while there is some random scattering, the

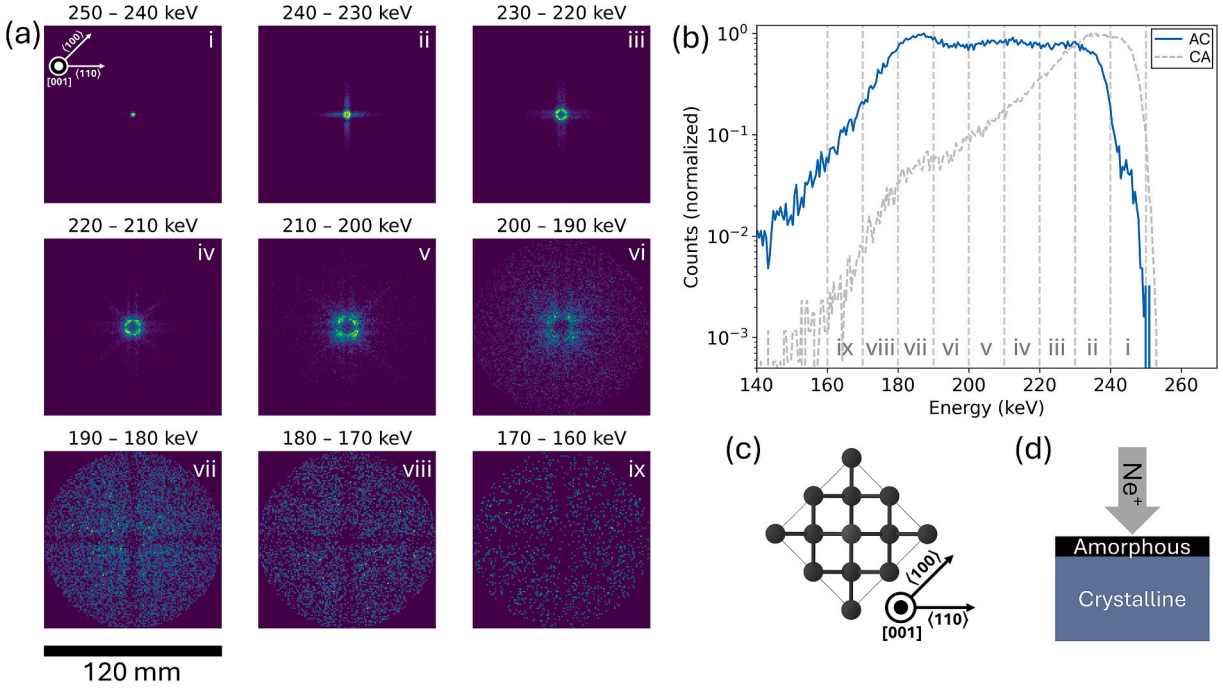

Fig. 3. IMSIL simulation results for the AC configuration with 280 keV $^{22}Ne^{+}$ beam (10^5 ions simulated). (a) Each sub-figure represents a 10 keV bin from (b) the energy spectrum (500 eV binning); dashed grey line in (b) is CA configuration shown here for comparison. NOTE: the color scale is unique to each subfigure. (c) Shows the crystal structure of the Si sample as seen from the perspective of the beam. (d) Shows the orientation of the sample in cross-section relative to the beam.

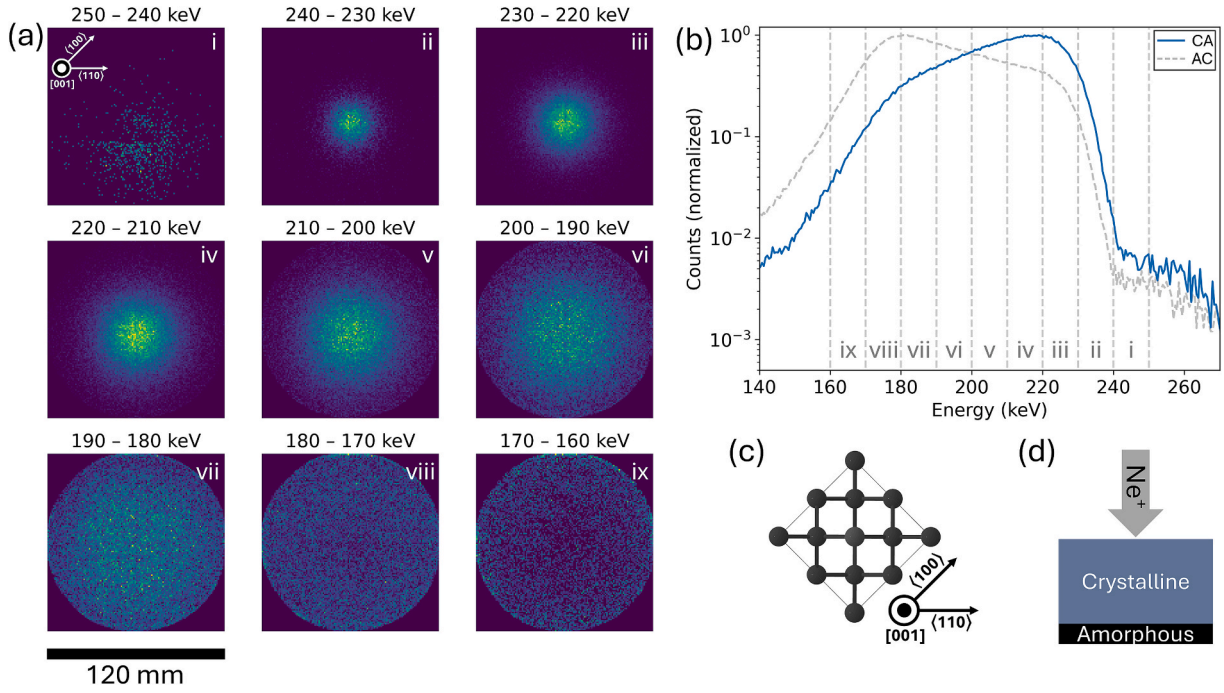

Fig. 4. Experimental results for the CA configuration with 280 keV $^{22}Ne^{+}$ beam. (a) Each sub-figure represents a 10 keV bin from (b) the energy spectrum (500 eV binning); dashed grey line in (b) is AC configuration shown here for comparison. Some of the counts in (i) are from stray particles which passed around the sample. NOTE: the color scale is unique to each subfigure. (c) Shows the crystal structure of the Si sample as seen from the perspective of the beam. (d) Shows the orientation of the sample in cross-section relative to the beam.

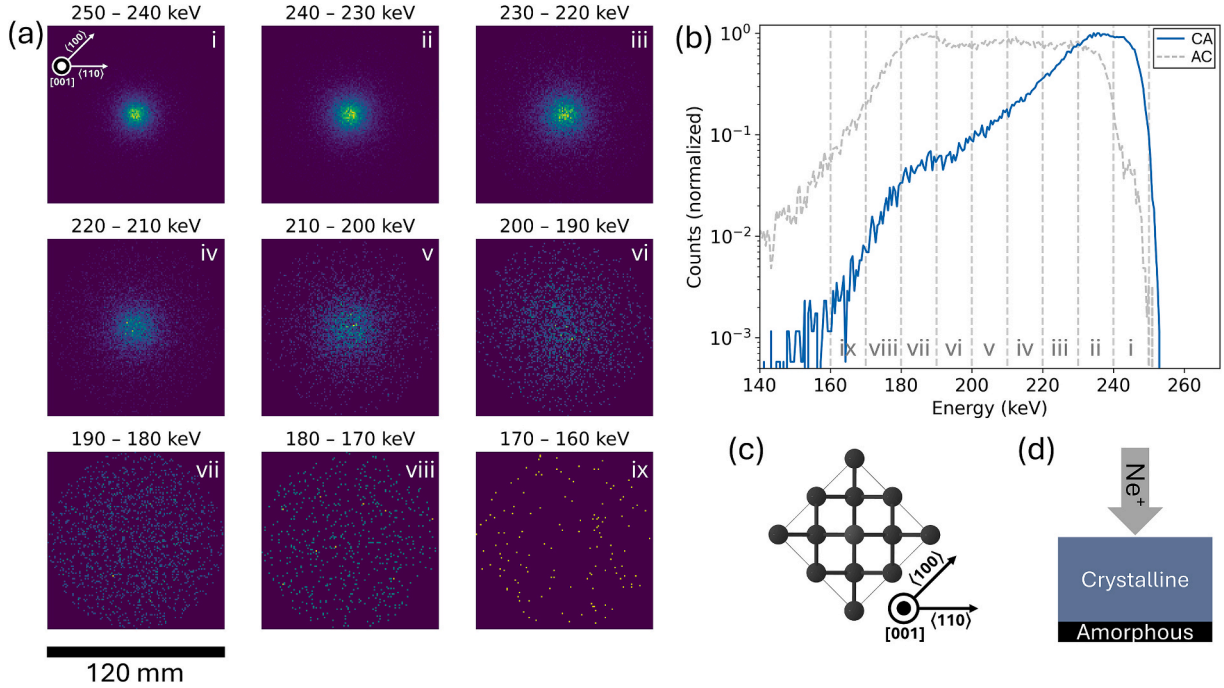

Fig. 5. IMSIL simulation results for the CA configuration with 280 keV $^{22}Ne^{+}$ beam (10^{5} ions simulated). (a) Each sub-figure represents a 10 keV bin from (b) the energy spectrum (500 eV binning); dashed grey line in (b) is AC configuration shown here for comparison. NOTE: the color scale is unique to each subfigure. (c) Shows the crystal structure of the Si sample as seen from the perspective of the beam. (d) Shows the orientation of the sample in cross-section relative to the beam.

majority of the particles remain channeled until reaching the amorphous layer.

Fig. 6c,d show angular spectrograms as a function of depth in the virtual sample. Fig. 6c shows that the transverse component of the ion trajectories is initially randomized by the amorphized layer, but that the ions are redirected into the planar channels once they enter the crystalline layer. The central dip in intensity at the major crystal axes is due to blocking. The periodic patterns in Fig. 6d highlight the features that emerge in the transmission pattern due to the oscillatory motion of the ions in the channels (see, e.g., rainbow channeling [44]). Once the ions reach the amorphous layer, they are scattered randomly, and no pattern is seen in the angular spectrogram.

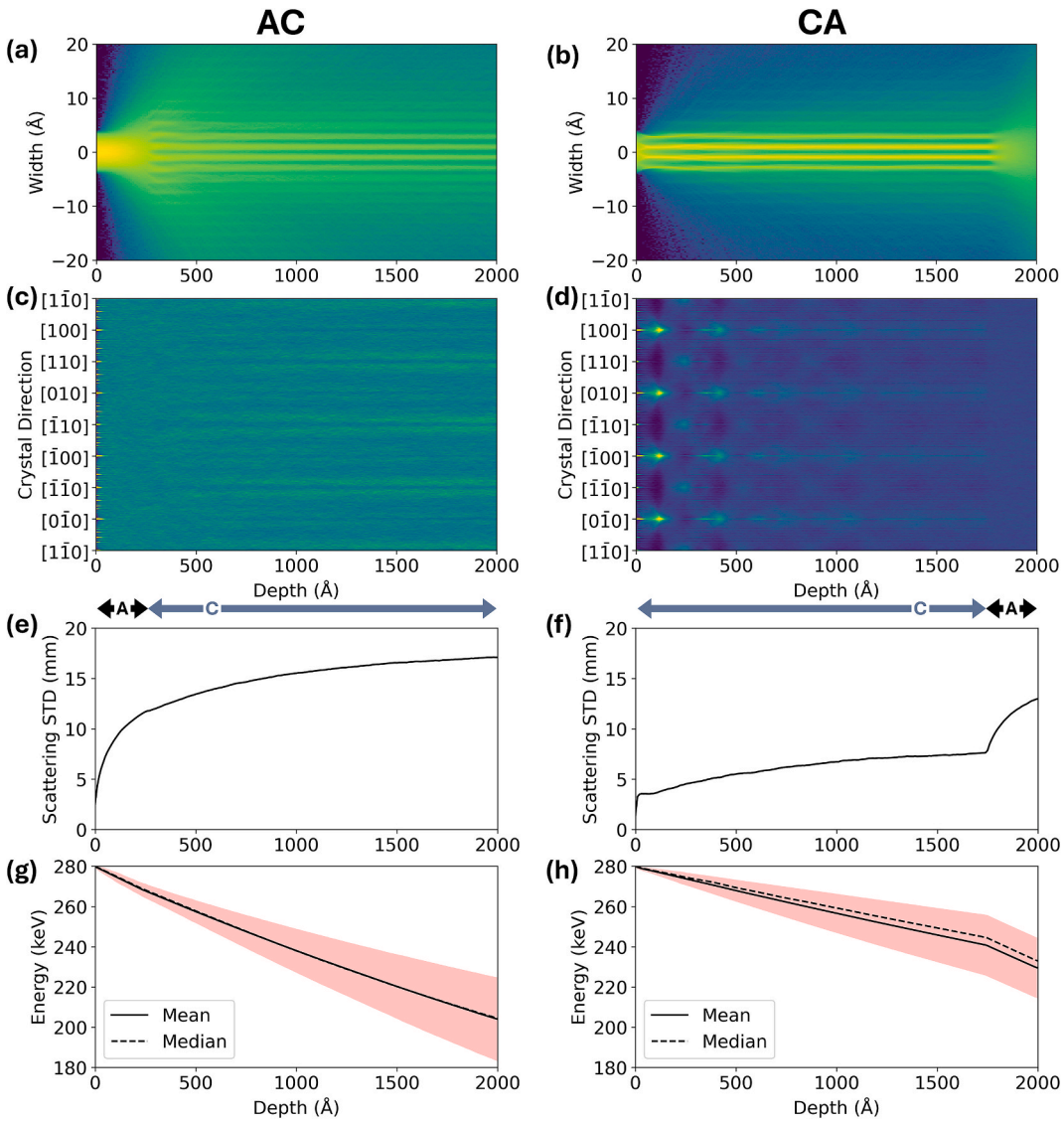

Fig. 6. Summary of the ^{22}Ne particle trajectories and energies as a function of depth in the sample for 10^5 simulated ions. (a,c,e,g) represent the data from the AC virtual sample, while (b,d,f,h) represent the data from the CA virtual sample. (a,b) are 2D histograms of the particle positions as seen from the [110] direction. (c,d) are crystal direction spectrograms, showing the scattering intensity into certain angles (3° bins). (e,f) are the standard deviation of the scattering position of the ions as seen from the detector. Finally, (g,h) track the average particle energy and standard deviation (red band) as seen on the detector. NOTE: The arrows above (e,f) indicate the region of the virtual sample which is amorphous vs. crystalline.

Fig. 6e,f show the standard deviation of the intensity distribution on the detector as a function of depth in the sample. While the data is not Gaussian, the standard deviation acts as a useful proxy for the scattering distribution on the detector. Fig. 6e shows a roughly logarithmic increase in standard deviation of the scattering pattern (this is influenced by the fact that ions falling outside of the detector area are not included), with significant scattering occurring before reaching the crystalline layer. Fig. 6f shows that the scattering increases precipitously at the transition between the crystalline and amorphous regions in the CA configuration.

Finally, Fig. 6g,h show the average particle energy and standard deviation as seen on the virtual detector as a function of the depth in the sample. The slope of the curve in Fig. 6g is much higher than that of Fig. 6h within the crystalline region, indicating greater energy-loss per unit depth in the crystalline region of the virtual sample for the AC configuration than the CA configuration. This is consistent with the hypothesis that the ions travel in pathways of higher energy loss on average after being scattered by the amorphous surface layer. In addition, the standard deviation of the energy is larger for the AC configuration. The mean and median curves are coincident for the AC configuration, indicating a symmetric distribution. For the CA configuration, however, the median is higher than the mean, indicating a skewed distribution where a relatively large fraction of the ions has lost less energy than the mean value. This skew comes from the fact that most ions stay channeled while a small fraction are randomly scattered.

Fig. 7 shows a schematic summary of the proposed mechanism for the effect seen in this paper: namely that the presence of an amorphous layer on one side of a thin membrane significantly impacts both the spatial and energy distribution of the transmitted particles depending on whether it is on the incident side (AC) or the exiting side (CA). The inset spectra demonstrate representative energy distributions of the various trajectories within the sample (though it is not possible to fully decouple the trajectories), created by choosing a region of interest (ROI) from the detector image associated with that trajectory (e.g. the pattern center for axial, arms of the star for planar, and neither for random). The spectra seen in Fig. 7 come from ROIs chosen from the experimental data shown in Fig. 2, but are only shown to illustrate the decomposition of the multimodal distribution.

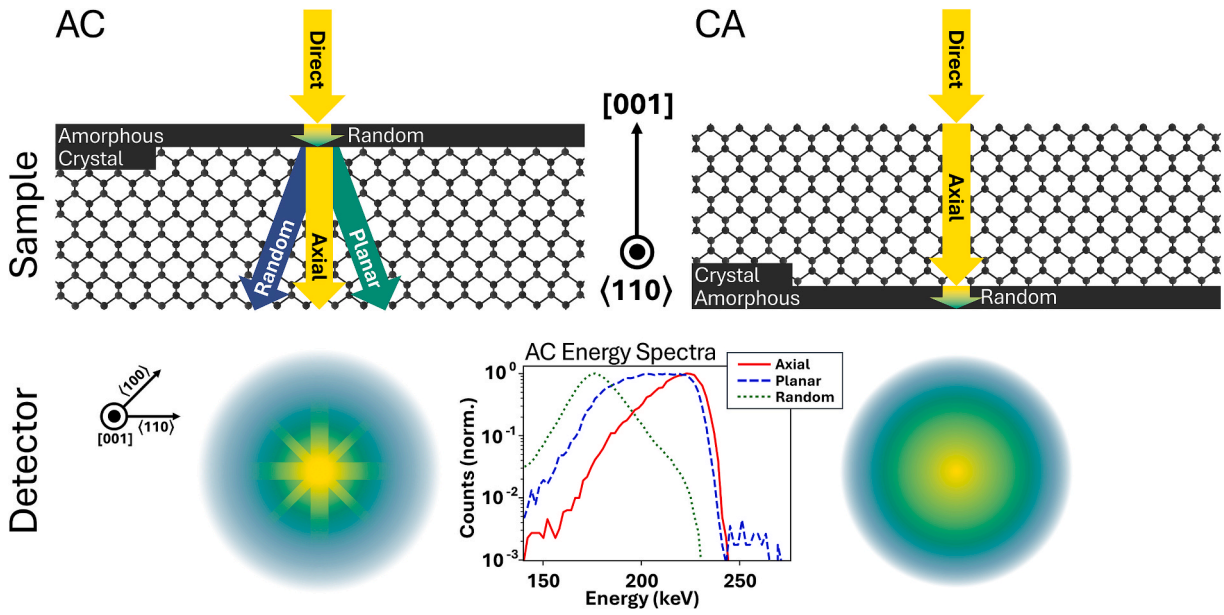

Fig. 7. Schematic showing the difference in the scattering in the AC configuration and the CA configuration. For the AC, the ions are scattered randomly in the amorphous layer, but some fraction is rechanneled in the crystalline layer along the axial and planar channels, leading to a distinctly crystalline transmission pattern. On the other hand, for the CA configuration, the ions pass mostly undisturbed through the crystalline layer, but are scattered randomly in the amorphous layer, leading to a radially uniform diffuse scattering pattern. INSET: The inset spectra (2 keV bins) show a decomposed version of the experimental energy spectrum for the AC configuration (see Fig. 2b), created by selecting regions on the detector representative of axial, planar, and random scattering trajectories. These spectra are shown for illustrative purposes only.

4. Conclusions

Comparing experimental and simulation results for both cases, i.e., the amorphous surface layer either facing the ion beam (AC configuration) or not (CA configuration), there is excellent qualitative but not fully quantitative agreement. The discrepancies are consistent with the idealized assumption of perfect crystallinity of the C layer in the simulations. The results from both the simulation and the experiment lead to the unintuitive conclusion that the transmission pattern with apparently random scattering has a smaller energy spread and less average energy loss, while the transmission pattern with a distinct crystalline pattern has a larger energy spread and greater average energy loss. This apparent paradox is solved in the following way: in both the AC and the CA configuration of the sample, the ions lose similar energy passing through the amorphous surface layer (see Fig. 6g,h); however, in the CA case the ions lose relatively little energy traveling along the [0 0 1] axial channel of the sample before being randomly scattered by the amorphous layer, while in the AC configuration the amorphous layer redirects many ions into higher energy loss paths, such as planar channels and random directions. The difference in energy loss for the [1 0 0] axial, {2 2 0} planar, and {4 0 0} planar channels can be attributed to the differences in the electronic stopping power along these directions in the crystal. Furthermore, the full-trajectory simulations corroborate the inferences made from the scattering patterns and energy spectra of the transmitted ion data.

Within this manuscript we only show results for ion beams aligned to the [0 0 1] axis of the crystal, however, some conclusions can be inferred about what may happen for various tilts. For tilts that are very close to the zone axis (i.e. within the critical acceptance angle), it is likely that there would be very little difference. The features in transmission patterns seen for small tilts of thin high-quality crystals (e.g. doughnut shapes [45]) are obscured by the scattering in the amorphous layer. Holeňák et al. have recently reported the impact of thin amorphous layers (in AC configuration) on the energy-loss spectra and transmission patterns for 100 keV Si transmitted through 50 nm Si membranes. For a random tilt, the amorphous layer directs a larger fraction of the particles into the channels, thus reducing their energy loss [22]. This is the opposite of what is seen for the axial configuration in this work, where the surface amorphous layer directs ions away from the axial channel and into higher energy-loss trajectories.

While the results appear consistent for different ions of similar velocity (see $^{4}He^{+}$ results in the *Supplementary Material* – Appendix D), it should be emphasized that they may not hold for significantly different ratios of the amorphous and crystalline layers (in this work between 10 % to 25 % of the membrane is expected to have been amorphized), or for significantly different particle velocities. These results are of particular interest for potential applications of transmitted ion microscopy in the keV range for more complex structures, which may have both amorphous and crystalline layers (such as semiconductor heterostructures, geological specimens, and thin film coatings). In such cases, the order of the layers can impact the interpretation of both the scattering and energy-loss results.

CRediT authorship contribution statement

Dustin Andersen: Writing – review & editing, Writing – original draft, Visualization, Software, Methodology, Investigation. **Radek Holeňák:** Writing – review & editing, Methodology, Investigation. **Saba Tabean:** Writing – review & editing, Investigation. **Eleni Ntemou:** Writing – review & editing, Methodology, Investigation. **Tom Wirtz:** Writing – review & editing, Project administration. **Gerhard Hobler:** Writing – review & editing, Software, Investigation. **Daniel Primetzhofer:** Writing – review & editing, Resources, Project administration, Funding acquisition. **Santhana Eswara:** Writing – review & editing, Supervision, Funding acquisition, Conceptualization.

Author Rights Retention

Declaration of competing interest

The authors declare that they have no known competing financial interests or personal relationships that could have appeared to influence the work reported in this paper.

Acknowledgements

The authors acknowledge funding from the Luxembourg National Research Fund (FNR) AIMSTHIM2 (C21/MS/16215748) for the experimental work performed at LIST, as well as funding from the EU Horizon 2020 program through the RADIATE project for the experimental work performed at Uppsala University. Accelerator operation at Uppsala University is supported by the Swedish Research Council VR-RFI (contract #2019_00191). The data and structure viewer of The Materials Project (www.materialsproject.org) was used for the illustrations of the Si crystal structure (mp-149).

Appendix A. Pristine samples and experimental data processing artifacts

Below are shown the channeling patterns for the pristine samples. Fig. A1a shows a pristine sample from the batch used for the experiments within this paper. The presence of the star pattern indicates that it may have a lower surface or crystal quality than that of the sample shown in Fig. A1b, which is from a different vendor, but has the same nominal properties (i.e., 200 nm thick single-crystal Si with tensile strain to maintain flatness). Finally, Fig. A1c shows the pristine sample as simulated with IMSIL for 10^5 ions. Fig. A2 shows the artifacts seen in the experimental patterns from the processing of the data.

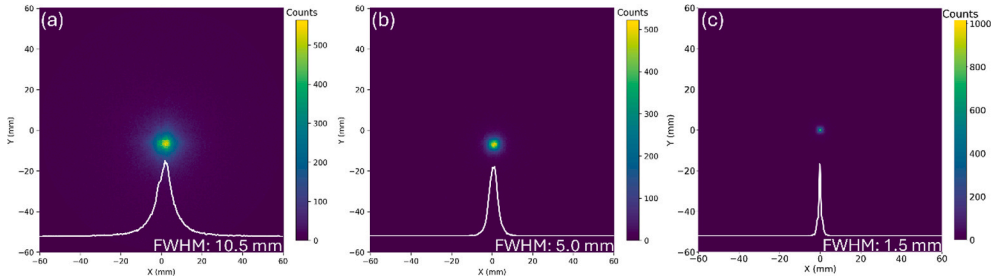

Fig. A1. Images showing the $< 001 >$ channeling/scattering pattern for 280 keV $^{22}Ne^{+}$ from (a) a pristine sample from the vendor used for the experiments in this paper, (b) a pristine sample from another vendor, (c) a pristine virtual sample simulated with IMSIL. Note that the channeling pattern for (a) sample is more diffuse and has a star-like pattern, indicating that this sample may have a lower crystal or surface quality. Line profiles are overlaid for each plot along with full-width half-maximum calculated from a Gaussian fit in OriginPro 2019b.

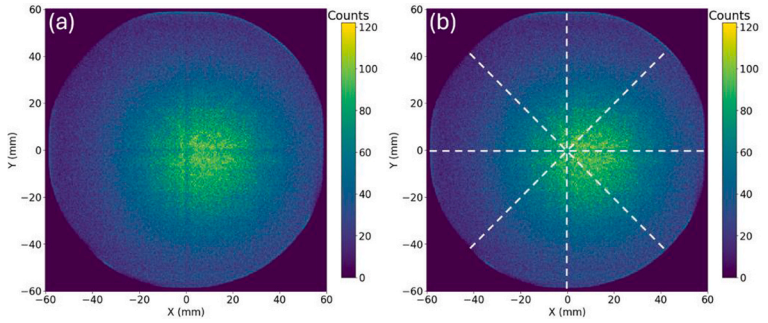

Fig. A2. Data shown as an example of the lines which appear on the detector images as an artifact of the data processing. (a) shows the data as collected and (b) highlights the position of the lines.

Appendix B. Experimental data treatment

The experimental data at the ToF-MEIS in Uppsala is recorded in the Roentdek Listmode file format, which can be analyzed by the program CoboldPC (COmputer Based On-line offline Listmode Dataanalyser). This data was exported to a space-delineated text format, where each line represents a set of events (e.g. particles hitting the detector) at a fixed time (up to 4 events), and each event has an XY position on the detector and a relative time as recorded by the TDC (i.e., from beam pulse to particle detection). However, secondary, tertiary, and quaternary events may sometimes be caused by ringing in the electronics, and so only the first events have been kept in the data set.

Appendix C. Full-trajectory simulation data

The figures below show the full-trajectory simulations for $^{22}Ne^{+}$ (see online version of this manuscript for videos). The still frames shown below in the offline version of the manuscript have been chosen to best highlight the salient features of the patterns which emerge in the videos. The images are 256×256 pixels, and the energy histograms have 100 bins from 0 to 280 keV (i.e., 2.8 keV per bin). Fig. C1 and Fig. C2 show the detector image and energy distribution if the crystal abruptly ended at the thickness given at the top of the figure (i.e. as if the instantaneous ion trajectories were projected onto the detector from that depth in the sample) for the AC configuration and the CA configuration of the sample, respectively. Fig. C3 and Fig. C4 show the position of the ions within the sample for the AC configuration at the given depth for a field of view of 40 Å and 400 Å, respectively, and Fig. C5 shows the same for the CA configuration. The significant increase in the number of low-energy ions in the energy spectra of Fig. C3-5

compared to the spectra of Fig. C1-2 is because all ions that scatter outside of a 60 mm radius are excluded from the detector images and their energy spectra. Finally, Fig. C6 and Fig. C7 show the energy of the ions as a function of position within the sample for both a 40 Å and 400 Å field of view, correlating the relative energy loss to the trajectories within the sample.

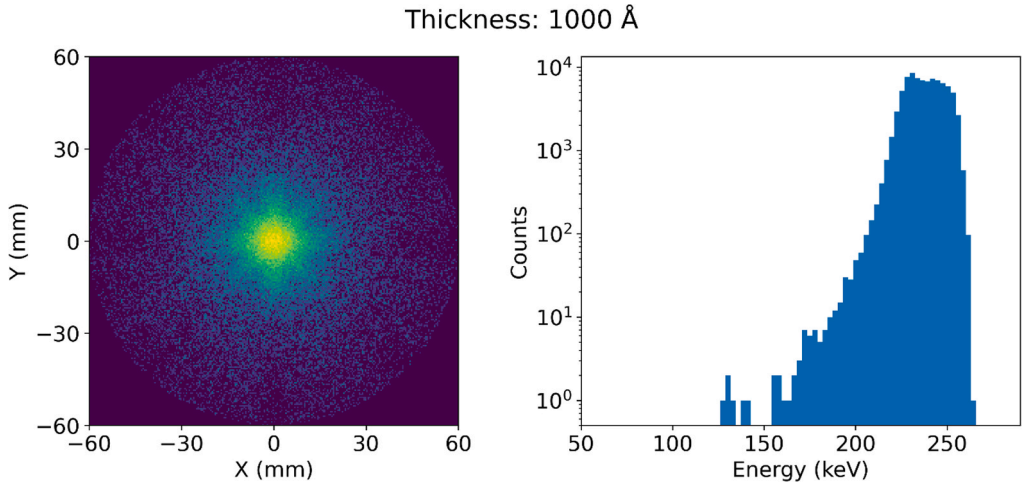

Fig. C1. (Left) Series of detector scattering images (120 mm field of view) and (Right) energy spectra as a function of depth through the virtual sample in the AC configuration. The transition from the amorphous to crystalline layer occurs at 250 Å. NOTE: Please refer to the online version of this manuscript for the animation.

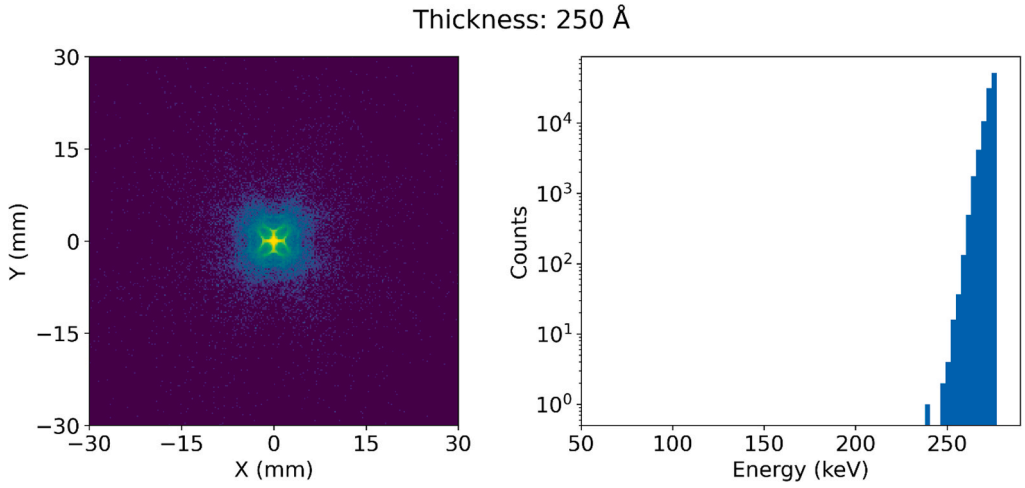

Fig. C2. (Left) Series of detector scattering images (60 mm field of view) and (Right) energy spectra as a function of depth through the virtual sample in the CA configuration. The evolution of the rainbow channeling pattern can be seen. The transition from the amorphous to crystalline layer occurs at 1750 Å. NOTE: Please refer to the online version of this manuscript for the animation.

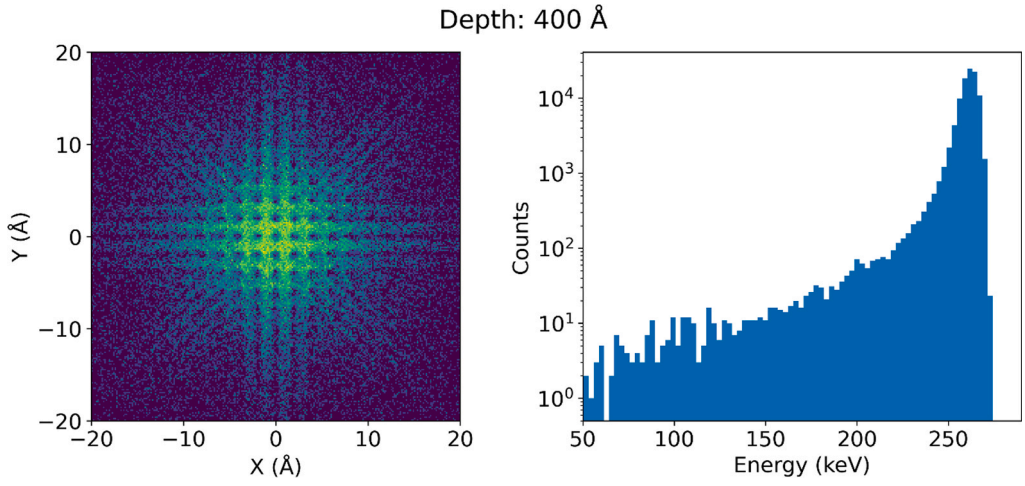

Fig. C3. (Left) Series of images showing the particle position (40 Å field of view) and (Right) energy spectra as a function of depth through the virtual sample in the AC configuration. The "holes" in the pattern correspond to the atomic columns. The transition from the amorphous to crystalline layer occurs at 250 Å. NOTE: Please refer to the online version of this manuscript for the animation.

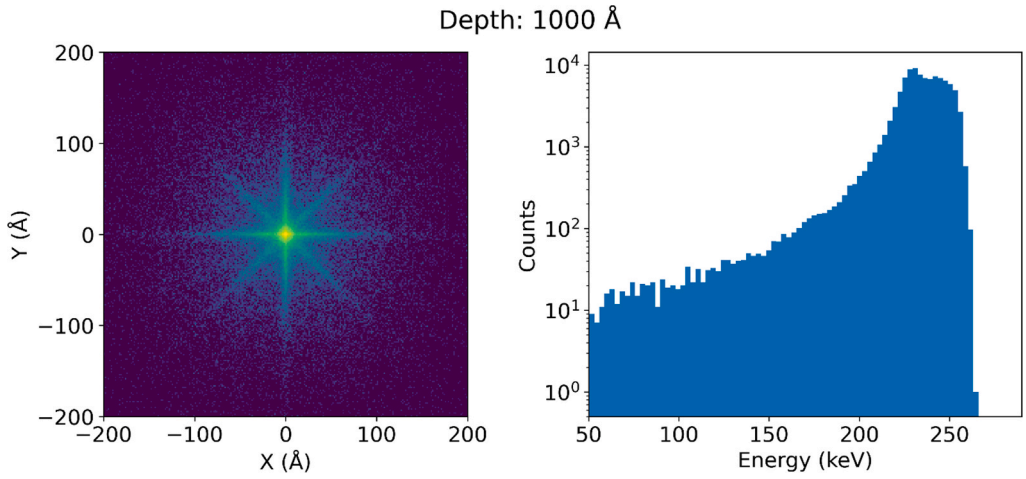

Fig. C4. (Left) Series of images showing the particle position (400 Å field of view) and (Right) energy spectra as a function of depth through the virtual sample in the AC configuration. The "arms" in the pattern correspond to the ions traveling along planar channels. The transition from the amorphous to crystalline layer occurs at 250 Å. NOTE: Please refer to the online version of this manuscript for the animation.

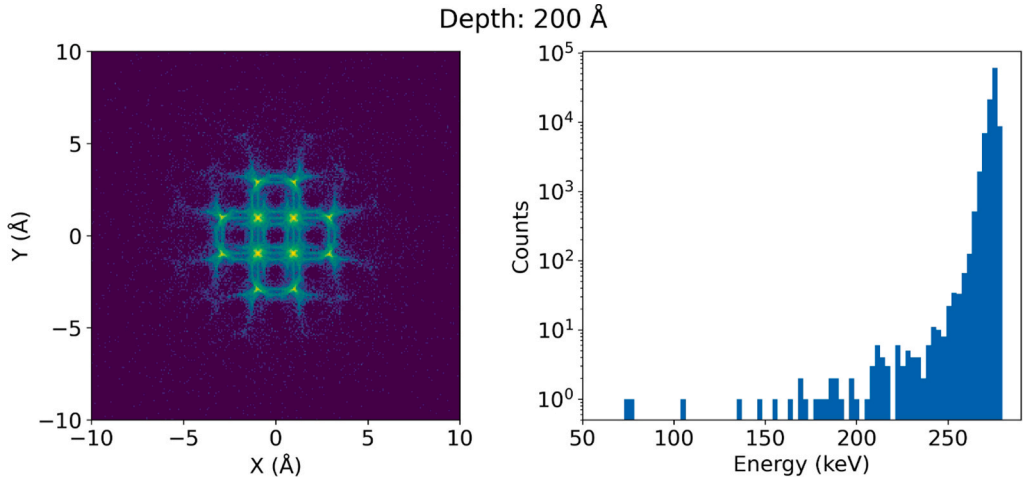

Fig. C5. (Left) Series of images showing the particle position (20 Å field of view) and (Right) energy spectra as a function of depth through the virtual sample in the CA configuration. It is possible to see the oscillatory motion along the axial channels that leads to the rainbow channeling patterns. The transition from the amorphous to crystalline layer occurs at 1750 Å. NOTE: Please refer to the online version of this manuscript for the animation.

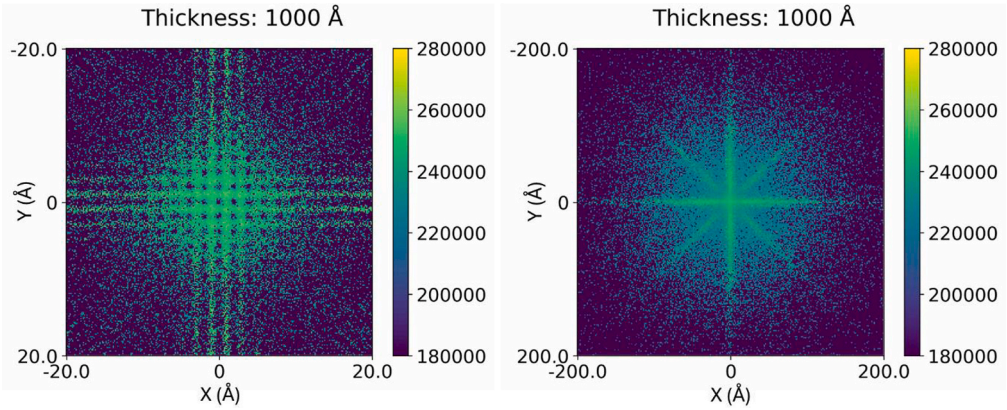

Fig. C6. Series of images showing the particle position (Left: 40 Å field of view; Right: 400 Å field of view), where the intensity is the average particle energy as a function of depth through the virtual sample in the AC configuration. (Left) the "holes" in the pattern correspond to the atomic columns. (Right) The "arms" in the pattern correspond to the ions traveling along planar channels. Note the difference in average energy for the various trajectories. The transition from the amorphous to crystalline layer occurs at 250 Å. NOTE: Please refer to the online version of this manuscript for the animation.

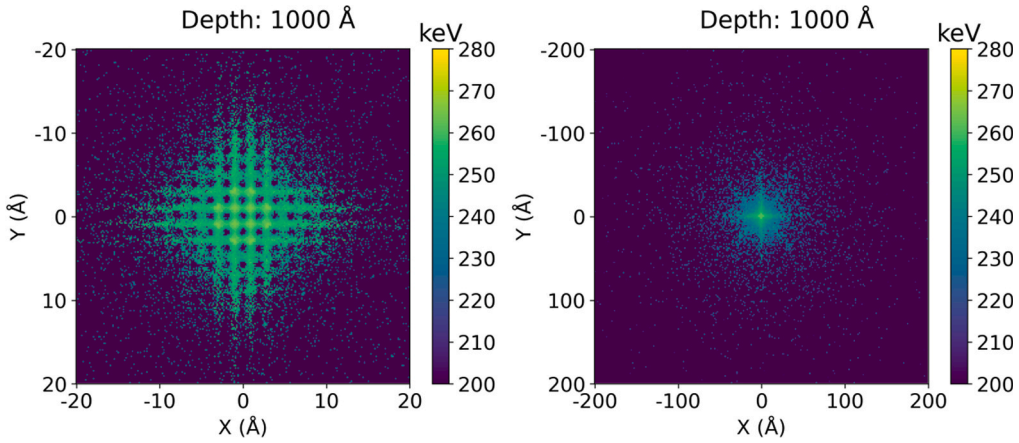

Fig. C7. Series of images showing the particle position (Left: 40 Å field of view; Right: 400 Å field of view), where the intensity is the average particle energy as a function of depth through the virtual sample in the CA configuration. (Left) the "holes" in the pattern correspond to the atomic columns. The transition from the amorphous to crystalline layer occurs at 1750 Å. NOTE: Please refer to the online version of this manuscript for the animation.

Appendix D. Supplementary data

Supplementary data to this article can be found online at https://doi.org/10.1016/j.apsusc.2025.163734.

Data availability

The raw data used for both the experimental and simulation results is available at https://doi.org/10.5281/zenodo.15658828.

References

[1] N. Bohr, The penetration of atomic particles through matter, Det K. Dan. Vidensk. Selsk. Mat.-Fys. Meddelelser 18 (8) (1948) 1–144.
[2] J. Lindhard, M. Scharff, Energy Dissipation by Ions in the kev Region, Phys. Rev. 124 (1961) 128–130, https://doi.org/10.1103/PhysRev.124.128.
[3] W.J. Weber, D.M. Duffy, L. Thomé, Y. Zhang, The role of electronic energy loss in ion beam modification of materials, Curr. Opin. Solid State Mater. Sci. 19 (2015) 1–11, https://doi.org/10.1016/j.cossms.2014.09.003.
[4] J. Lindhard, M. Scharff, Energy loss in matter by fast particles of low charge, Det K. Dan. Vidensk. Selsk. Mat.-Fys. Meddelelser 27 (15) (1953) 1–31.
[5] Y. Bandurin, S. Lacombe, L. Guillemot, V.A. Esaulov, Surface plasmon excitation in hydrogen and helium ion scattering on Ag, Surf. Sci. 513 (2002) L413–L418, https://doi.org/10.1016/S0039-6028(02)01568-6.
[6] M. Caro, A.A. Correa, E. Artacho, A. Caro, Stopping power beyond the adiabatic approximation, Sci. Rep. 7 (2017) 2618, https://doi.org/10.1038/s41598-017-02780-3.
[7] J. Lindhard, Influence of crystal lattice on motion of energetic charged particles, Det K. Dan. Vidensk. Selsk. Mat.-Fys. Meddelelser 34 (14) (1965) 1–64.
[8] G. Hobler, Critical angles and low-energy limits to ion channeling in silicon, Radiat. Eff. Defects Solids 139 (1996) 21–85, https://doi.org/10.1080/10420159608212927.
[9] E.V. Kornelsen, F. Brown, J.A. Davies, B. Domeij, G.R. Piercy, Penetration of heavy ions of keV energies into monocrystalline tungsten, Phys. Rev. 136 (1964) A849–A858, https://doi.org/10.1103/PhysRev.136.A849.
[10] M.T. Robinson, O.S. Oen, Computer studies of the slowing down of energetic atoms in crystals, Phys. Rev. 132 (1963) 2385–2398, https://doi.org/10.1103/PhysRev.132.2385.
[11] K. Nordlund, F. Djurabekova, G. Hobler, Large fraction of crystal directions leads to ion channeling, Phys. Rev. B 94 (2016) 214109, https://doi.org/10.1103/PhysRevB.94.214109.
[12] H.F. Krause, S. Datz, P.F. Dittner, J. Gomez del Campo, P.D. Miller, C.D. Moak, N. Nešković, P.L. Pepmiller, Rainbow effect in axial ion channeling, Phys. Rev. B 33 (1986) 6036–6044, https://doi.org/10.1103/PhysRevB.33.6036.
[13] S. Petrović, L. Miletić, N. Nešković, Theory of rainbows in thin crystals: The explanation of ion channeling applied to Ne10+ ions transmitted through a⟨100⟩ Si thin crystal, Phys. Rev. B 61 (2000) 184–189, https://doi.org/10.1103/PhysRevB.61.184.
[14] M.B.H. Breese, E.J. Teo, L. Huang, A review of transmission channelling using high-demagnification microprobes, Nucl. Instrum. Methods Phys. Res. Sect. B Beam Interact. Mater. At. 260 (2007) 288–292, https://doi.org/10.1016/j.nimb.2007.02.110.
[15] J.A. Davies, J. Denhartog, J.L. Whitton, Channeling of MeV projectiles in tungsten and silicon, Phys. Rev. 165 (1968) 345–356, https://doi.org/10.1103/PhysRev.165.345.
[16] J.U. Andersen, Channeling and blocking of energetic charged particles in crystals, Det K. Dan. Vidensk. Selsk. Mat.-Fys. Meddelelser 52 (2) (2006) 655–698.
[17] J.U. Andersen, O. Andreasen, J.A. Davies, E. Uggerhj, The use of channeling-effect techniques to locate interstitial foreign atoms in silicon, Radiat. Eff. 7 (1971) 25–34, https://doi.org/10.1080/00337577108232561.
[18] S.T. Picraux, J.A. Davies, L. Eriksson, N.G.E. Johansson, J.W. Mayer, Channeling studies in diamond-type lattices, Phys. Rev. 180 (1969) 873–882, https://doi.org/10.1103/PhysRev.180.873.
[19] T.M. Liu, W.G. Oldham, Shallow boron junctions implanted in silicon through a surface oxide, IEEE Electron Device Lett. 5 (1984) 299–301, https://doi.org/10.1109/EDL.1984.25924.
[20] C. Park, K.M. Klein, A.F. Tasch, R.B. Simonton, G.E. Lux, Paradoxical boron profile broadening caused by implantation through a screen oxide layer, in: International Electron Devices Meeting 1991 [Technical Digest], IEEE, 1991, pp. 67–70, https://doi.org/10.1109/IEDM.1991.235422.
[21] G. Hobler, H. Pötzl, The effect of a screening oxide on ion implantation studied by Monte Carlo simulations, COMPEL - Int J. Comput. Math. Electr. Electron. Eng. 11 (1992) 403–411, https://doi.org/10.1108/eb010101.
[22] R. Holeňák, E. Ntemou, S. Lohmann, M. Linnarsson, D. Primetzhofer, Assessing trajectory-dependent electronic energy loss of keV ions by a binary collision approximation code, Phys. Rev. Appl. 21 (2024) 024048, https://doi.org/10.1103/PhysRevApplied.21.024048.
[23] R. Mikšová, A. Macková, A. Jagerová, P. Malinský, P. Slepička, V. Švorčík, Structural study and ion-beam channelling in Si ⟨1 0 0⟩ modified by Kr+, Ag+, 2+ and Au+, 2+ ions, Appl. Surf. Sci. 458 (2018) 722–733, https://doi.org/10.1016/j.apsusc.2018.07.118.
[24] G. Hlawacek, V. Veligura, R. Van Gastel, B. Poelsema, Helium ion microscopy, J. Vac. Sci. Technol. B Nanotechnol. Microelectron. Mater. Process. Meas. Phenom. 32 (2014) 020801, https://doi.org/10.1116/1.4863676.
[25] S. Tabean, M. Mousley, C. Pauly, O. De Castro, E. Serralta, N. Klingner, F. Mücklich, G. Hlawacek, T. Wirtz, S. Eswara, Quantitative nanoscale imaging using transmission He ion channelling contrast: Proof-of-concept and application to study isolated crystalline defects, Ultramicroscopy 233 (2022) 113439, https://doi.org/10.1016/j.ultramic.2021.113439.
[26] J.F. Ziegler, M.D. Ziegler, J.P. Biersack, SRIM – The stopping and range of ions in matter (2010), Nucl. Instrum. Methods Phys. Res. Sect. B Beam Interact. Mater. At. 268 (2010) 1818–1823, https://doi.org/10.1016/j.nimb.2010.02.091.
[27] A.V. Rumyantsev, A.S. Prikhodko, N.I. Borgardt, Study of gallium-ion-induced silicon amorphization by matching experimental and simulated electron-microscopy images, J. Surf. Investig. X-Ray Synchrotron Neutron Tech. 14 (2020) 956–960, https://doi.org/10.1134/S1027451020050171.
[28] A.V. Rumyantsev, N.I. Borgardt, A.S. Prikhodko, Y.A. Chaplygin, Characterizing interface structure between crystalline and ion bombarded silicon by transmission electron microscopy and molecular dynamics simulations, Appl. Surf. Sci. 540 (2021) 148278, https://doi.org/10.1016/j.apsusc.2020.148278.
[29] M. Kolíbal, T. Matlocha, T. Vystavěl, T. Šikola, Low energy focused ion beam milling of silicon and germanium nanostructures, Nanotechnology 22 (2011) 105304, https://doi.org/10.1088/0957-4484/22/10/105304.
[30] C.N. Shyam Kumar, S. Tabean, A. Morisset, P. Wyss, M. Lehmann, F.-J. Haug, Q. Jeangros, A. Hessler-Wyser, N. Valle, T. Wirtz, S. Eswara, Evaluation of secondary electron intensities for dopant profiling in ion implanted semiconductors: a correlative study combining SE, SIMS and ECV methods,

Semicond. Sci. Technol. 36 (2021) 085003, https://doi.org/10.1088/1361-6641/ac0854.
[31] Y.J. Xiao, F.Z. Fang, Z.W. Xu, W. Wu, X.C. Shen, The study of Ga+ FIB implanting crystal silicon and subsequent annealing, Nucl. Instrum. Methods Phys. Res. Sect. B Beam Interact. Mater. At. 307 (2013) 253–256, https://doi.org/10.1016/j.nimb.2012.12.112.
[32] S. Lohmann, R. Holeňák, D. Primetzhofer, Trajectory-dependent electronic excitations by light and heavy ions around and below the Bohr velocity, Phys. Rev. A 102 (2020) 062803, https://doi.org/10.1103/PhysRevA.102.062803.
[33] M.K. Linnarsson, A. Hallén, J. Åström, D. Primetzhofer, S. Legendre, G. Possnert, New beam line for time-of-flight medium energy ion scattering with large area position sensitive detector, Rev. Sci. Instrum. 83 (2012) 095107, https://doi.org/10.1063/1.4750195.
[34] M.A. Sortica, M.K. Linnarsson, D. Wessman, S. Lohmann, D. Primetzhofer, A versatile time-of-flight medium-energy ion scattering setup using multiple delay-line detectors, Nucl. Instrum. Methods Phys. Res. Sect. B Beam Interact. Mater. At. 463 (2020) 16–20, https://doi.org/10.1016/j.nimb.2019.11.019.
[35] E. Ntemou, R. Holeňák, D. Wessman, D. Primetzhofer, Picosecond pulsed beams of light and heavy keV ions at the time-of-flight medium energy ion scattering system at Uppsala University, Nucl. Instrum. Methods Phys. Res. Sect. B Beam Interact. Mater. At. 556 (2024) 165494, https://doi.org/10.1016/j.nimb.2024.165494.
[36] S. Lohmann, D. Primetzhofer, Disparate energy scaling of trajectory-dependent electronic excitations for slow protons and He ions, Phys. Rev. Lett. 124 (2020) 096601, https://doi.org/10.1103/PhysRevLett.124.096601.
[37] S. Lohmann, M.A. Sortica, V. Paneta, D. Primetzhofer, Analysis of photon emission induced by light and heavy ions in time-of-flight medium energy ion scattering, Nucl. Instrum. Methods Phys. Res. Sect. B Beam Interact. Mater. At. 417 (2018) 75–80, https://doi.org/10.1016/j.nimb.2017.08.005.
[38] G. Hobler, Monte Carlo simulation of two-dimensional implanted dopant distributions at mask edges, Nucl. Instrum. Methods Phys. Res. Sect. B Beam Interact. Mater. At. 96 (1995) 155–162, https://doi.org/10.1016/0168-583X(94)00476-5.
[39] G. Hobler, IMplant and Sputter sImuLator (IMSIL), https://www.tuwien.at/en/etit/fke/research/process-simulation.
[40] G. Hobler, A. Simionescu, Acceleration of binary collision simulations in crystalline targets using critical angles for ion channeling, Nucl. Instrum. Methods Phys. Res. Sect. B Beam Interact. Mater. At. 102 (1995) 24–28, https://doi.org/10.1016/0168-583X(95)80111-X.
[41] J.F. Ziegler, J.P. Biersack, U. Littmark, The stopping and range of ions in solids, Pergamon, New York, 1985.
[42] G. Hobler, C.S. Murthy, Towards a comprehensive model of electronic stopping in amorphous and crystalline silicon, in: 2000 International Conference on Ion Implantation Technology Proceedings. Ion Implantation Technology-2000 (Cat. No. 00EX432), IEEE, 2000, pp. 209–212, https://doi.org/10.1109/IIT.2000.924126.
[43] R. Holeňák, S. Lohmann, K. Komander, D. Primetzhofer, On the correlation of angular distributions of keV ions and trajectory-dependent electronic excitations in transmission channelling geometry, in: Journal of Physics: Conference Series, Vol. 2326, No. 1, IOP Publishing, 2022, p. 012008, https://doi.org/10.1088/1742-6596/2326/1/012008.
[44] S. Petrović, S. Korica, M. Kokkoris, N. Nešković, Angular distributions of ions channeled in the⟨100⟩Si crystals, Nucl. Instrum. Methods Phys. Res. Sect. B Beam Interact. Mater. At. 193 (2002) 152–159, https://doi.org/10.1016/S0168-583X(02)00742-5.
[45] J.S. Rosner, W.M. Gibson, J.A. Golovchenko, A.N. Goland, H.E. Wegner, Quantitative study of the transmission of axially channeled protons in thin silicon crystals, Phys. Rev. B 18 (1978) 1066–1075, https://doi.org/10.1103/PhysRevB.18.1066.